CHALMERS
UNIVERSITY OF TECHNOLOGY

Probing the electrode-liquid interface using operando total-reflection X-ray absorption spectroscopy

Surface Science 748 (2024) 122538

Contents lists available at ScienceDirect

Surface Science

journal homepage: www.elsevier.com/locate/susc

Probing the electrode-liquid interface using *operando* total-reflection X-ray absorption spectroscopy

A. Grespi [a,b,*], A. Larsson [a,b], G. Abbondanza [c], J. Eidhagen [d], D. Gajdek [e,b], J. Manidi [f], A. Tayal [g], J. Pan [h], L.R. Merte [e,f], E. Lundgren [a,b]

[a] Division of Synchrotron Radiation Research, Lund University, Professorsgatan 1, Lund 22363, Sweden
[b] NanoLund, Lund University, Professorsgatan 1, Lund 22363, Sweden
[c] Department of Physics, Chalmers University of Technology, Chalmersplatsen 4, Gothenburg 41296, Sweden
[d] Alleima (former Sandvik Materials Technology), Sandviken, Sweden
[e] Materials Science and Applied Mathematics, Malmö University, Malmö 20506, Sweden
[f] Politecnico di Milano, Department of Chemistry, Materials and Chemical Engineering, G. Natta, Milano 20133, Italy
[g] Deutsches Elektronen-Synchrotron DESY, Notkestr. 85, Hamburg D-22607, Germany
[h] KTH Royal Institute of Technology, Division of Surface and Corrosion Science, Stockholm, Sweden

ARTICLE INFO

Keywords:
Solid/liquid interface
Total reflection X-ray absorption spectroscopy
Operando X-ray spectroscopy
Electrochemical refleXAFS
Passivity breakdown
Oxygen evolution reaction

ABSTRACT

Traditional methods to study electrochemical (EC) processes, although successful, are based on current/voltage measurements, providing information about performances rather than offering a direct observation of chemical and structural changes occurring at the electrode surface. These processes are localized at the electrode-electrolyte interface, the structure of which is the main determinant of their behavior, but most surface sensitive experimental techniques are limited to *ex situ* conditions, owing to the need for an ultra-high vacuum environment. In this contribution, we report *operando* X-ray absorption spectroscopy in total external reflection geometry (Refle-XAFS) at P64 beamline (DESY, Hamburg), using a simple and versatile EC flow cell designed for multimodal surface sensitive studies with hard X-ray scattering and spectroscopy techniques. We show that the Refle-XAFS method can be used to study chemical surface changes of industrial alloys and model electrodes in harsh electrochemical environments, without being limited to thin film samples. The surface passive film development and breakdown of a corrosion-resistant Ni-Cr-Mo alloy and the electro-oxidation of polycrystalline gold (poly-Au), relevant for fundamental studies on water electrolysis, were investigated. Despite the strong attenuation of the beam by the electrolyte and the PEEK walls of the EC cell, nanoscale surface oxide films were detected using beam energies down to 8 keV. The passivity breakdown region of Ni alloy 59 in 1 M NaCl at pH 7 and pH 12 was identified, showing differences in the composition of the surface oxides during anodic polarization. The electro-oxidation of poly-Au in 0.05 M H_2SO_4 was observed, showing a progression from two-dimensional $Au^{1+/3+}$ to three-dimensional thick Au^{3+} surface oxide/hydroxide during OER.

1. Introduction

Various fields of modern research and technology are linked to electrochemical (EC) phenomena, e.g. corrosion [1,2], electrocatalysis [3,4] and energy storage [5,6]. These processes involve charge separation and transfer at the interfaces, most often inducing chemical and structural changes to electrode surfaces region that can strongly affect the material properties [7–9]. EC measurements such as cyclic voltammetry (CV) or electrochemical impedance spectroscopy (EIS) are highly sensitive to such changes but do not directly identify chemical and structural modifications of the electrode-electrolyte interface. Complementary surface sensitive techniques, e.g. X-ray photoelectron spectroscopy (XPS), Auger electron spectroscopy (AES), low energy electron diffraction (LEED), are often limited to *ex situ* ultra-high vacuum (UHV) environments, due to a too small inelastic mean free path of the electrons and photo-electrons [2,10,11].

Real *operando* experiments on such systems can give new insights on the actual reaction mechanisms [9,12,13], but imply that measurements are performed while the sample is submerged in the electrolyte and under EC polarization. In these conditions a probing source that can

* Corresponding author at: Division of Synchrotron Radiation Research, Lund University, Professorsgatan 1, Lund 22363, Sweden.
E-mail address: andrea.grespi@sljus.lu.se (A. Grespi).

https://doi.org/10.1016/j.susc.2024.122538
Received 15 March 2024; Received in revised form 12 June 2024; Accepted 14 June 2024
Available online 17 June 2024

penetrate the electrolyte and carry out information without undergoing excessive attenuation is needed, such as a modern synchrotron-based hard X-ray source, characterized by an extremely high brilliance and photon energies ranging typically from around 10 keV to greater than 100 keV. In this energy range and below, the attenuation of X-rays through a medium is dominated by photoelectric absorption interactions, whose cross-section (probability) is proportional to E^{-3}, where E is the beam energy. As a result, the higher the X-ray beam energy, the lower is the attenuation of the beam by the electrolyte. Hence, soft X-rays based techniques are complicated by the high attenuation through air and electrolyte of low energy X-rays, similarly to electrons and photoelectrons based techniques [14–17].

Thus, a valuable option to perform successful *operando* measurements would be to use hard X-ray methods based on photon-in photon-out processes, where only high energy photons are involved. X-ray diffraction (XRD) is indeed a photon-in photon-out based technique and is not limited to low beam energies, but amorphous oxides are commonly formed at the electrode-electrolyte interfacial region during EC reactions, making a direct identification of species using diffraction based methods more complex [9,18,19]. As an alternative to XRD and XPS techniques, X-ray absorption spectroscopy (XAS) is a fingerprinting technique that can also be measured via photon-in photon-out processes, providing local structural and chemical information independently on the sample crystallinity [20].

Traditionally XAS is performed by scanning the incident beam energy through an absorption edge and measuring the transmitted beam intensity or the secondary fluorescence signal. However, transmission mode measurements are inherently bulk sensitive, as the beam probes all material in its path, and so they can only provide surface information for samples with very high specific surface areas, such as nanoparticles [21–24]. To achieve nanoscale surface sensitivity using synchrotron-based X-rays on a large flat surface, the beam can be focused and aligned at shallow incident angles, adopting a so-called grazing incidence (GI) geometry. In this configuration, our EC flow cell enables us to study features of surfaces at the nanoscale in *operando* conditions, using a multimodal approach based on hard X-rays and photon-in photon-out processes [9,18,25–27]. GI-XAS in fluorescence mode has provided a sufficiently high signal-to-noise ratio for nm-thin films samples grown on a substrate [28–35]. However, fluorescence mode works only if the element of interest is exclusively located at the surface, whilst too thick films, macroscopic defects or substrates containing the same element of the film can introduce bulk fluorescence signals and self-absorption phenomena [32,36].

A good choice in the case of thick samples, such as single crystals or industrial alloys, is to use a mirror polished surface and set the incident angle below the critical angle for total external reflection (TER) [37,38], to measure the totally reflected beam intensity as a function of the incident beam energy, also known as Refle-XAFS [39–53]. In this configuration the reflectivity of an ideally perfect flat surface is almost 100 % and the energy dependent reflectance R(E) in the vicinity of a core-level absorption edge is dominated by XAS features, revealing exclusively surface chemistry and atomic structure details down to a few nm depths, independently on the sample thickness. Differently from transmission and fluorescence modes XAS measurements, R(E) is affected by both the real and imaginary part of the energy dependent refractive index [$n(E) = 1 - \delta(E) - i\beta(E)$] of the surface, making the extraction of the absorption coefficient more complicated [43,45,46,49,51]. Furthermore, the information depth slightly changes with the energy, especially across the absorption edge, while roughness and clustering of the surface can affect the contribution of different components in the spectra [43,45,54]. Thus, an accurate estimation of the contribution of near-surface species and the surface roughness requires modelling of R(E), e.g. using the Fresnel theory and the distorted wave born approximation [38,39]. However, traditional data reduction with e.g. the Athena software, which is part of the IFEFFIT EXAFS data analysis software [55], has been shown to work for qualitatively identifying the main components on the surface and to follow the evolution of surface species in a semi-quantitative way [39].

The Refle-XAFS method has always been employed using deposited thin films on a substrate and it is not broadly adopted and well explored, especially in the case of *operando* EC studies where the signal-to-noise ratio is significantly reduced by electrolyte attenuation and only very high energy X-rays (tens of keV) were used [43,44,47]. In the past decades, these experimental complications resulted in demanding sample preparations and elaborated EC setups that were also often difficult to combine with other surface sensitive techniques. Thanks to recent developments in synchrotron radiation, better beam focus and stability and higher photon flux can provide a higher surface signal, opening new possibilities to synchrotron-based *operando* surface studies in EC environments.

In this contribution, we demonstrate that Refle-XAFS under electrochemical conditions can be performed at energies as low as 8 keV using a simple and versatile setup based on the same cylindrical cell used recently for multimodal measurements based on X-ray scattering techniques and surface optical reflectance (SOR) [9,18,25,27,56]. In contrast to previous studies using the Refle-XAFS technique, where sputtered films on large and flat substrates were studied, the results demonstrate that more relevant and easily-produced samples can be characterized in *operando* conditions as well on a modern high-brilliance synchrotron beamline. The capabilities and features of the technique are discussed along with two case-studies: A) The passive film development and breakdown of Ni alloy 59, a corrosion resistant Ni-Cr-Mo industrial alloy, whose corrosion behavior is related to its electrocatalytic activity towards the oxygen evolution reaction (OER) [9,16,57,58]. B) The electro-oxidation of a polycrystalline Au (poly-Au) electrode surface, to investigate the oxidation and degradation of model electrocatalysts during water electrolysis [17,59–61].

2. Materials and methods

Fig. 1 illustrates schematically the principle and layout of the Refle-XAFS setup for surface characterization under electrochemical conditions. As a result of TER, an evanescent wave propagates along the surface and its intensity I(y) decays exponentially towards the bulk. As shown in Fig. 1a, samples were hat-shaped to fit in the PEEK (poly- ether ketone) EC flow cell [56,62]. The top surface of each sample, where the beam impinges at a grazing angle such that TER occurs, was mirror polished as follows: a hat-shaped poly-Au with large grains (Fig. S1) and two Ni alloy 59 samples were fabricated and polished by Surface Preparation Laboratory (SPL, Netherlands) with an average roughness Ra $<$ 0.03 μm. Two other hat-shaped Ni alloy 59 samples were fabricated and polished by Alleima AB (Sweden), the polishing procedure is shown in supplementary information (Table S1). The elemental composition of Ni alloy 59 (Table S2 and S3) and the microstructure (Fig. S2) are shown in the supplementary information.

The diameter of the polished surfaces was 7.5 mm, while the inner diameter of the cell was 8 mm. The cell inner diameter defines the length of the path of the X-rays through the electrolyte, which is the main contributor to the beam attenuation during *operando* experiments. Furthermore, the beam is attenuated through the two 200 μm thick PEEK walls of the EC cell.

At the P64 Beamline [63] (DESY, Hamburg) the EC cell was mounted such that the normal to the sample surface was oriented along the y direction, within the working table plane, as shown in Fig. 2. Linear and tilt stages allowed sample translation and tilt along y-axis, a rotation stage allowed sample rotation around z-axis, to set the incident angle. Beam size was set to 150×150 μm [2] and beam energy was scanned across the investigated absorption edges, namely the K-edges of Mo (19.99 keV), and Ni (8.33 keV) and the L_3-edge of Au (11.92 keV). Attempts were also made to probe the Cr K-edge (5.99 keV), but this was not possible due to the excessive attenuation at this energy. At each of these energies, the critical angle was calculated for the Ni and Au

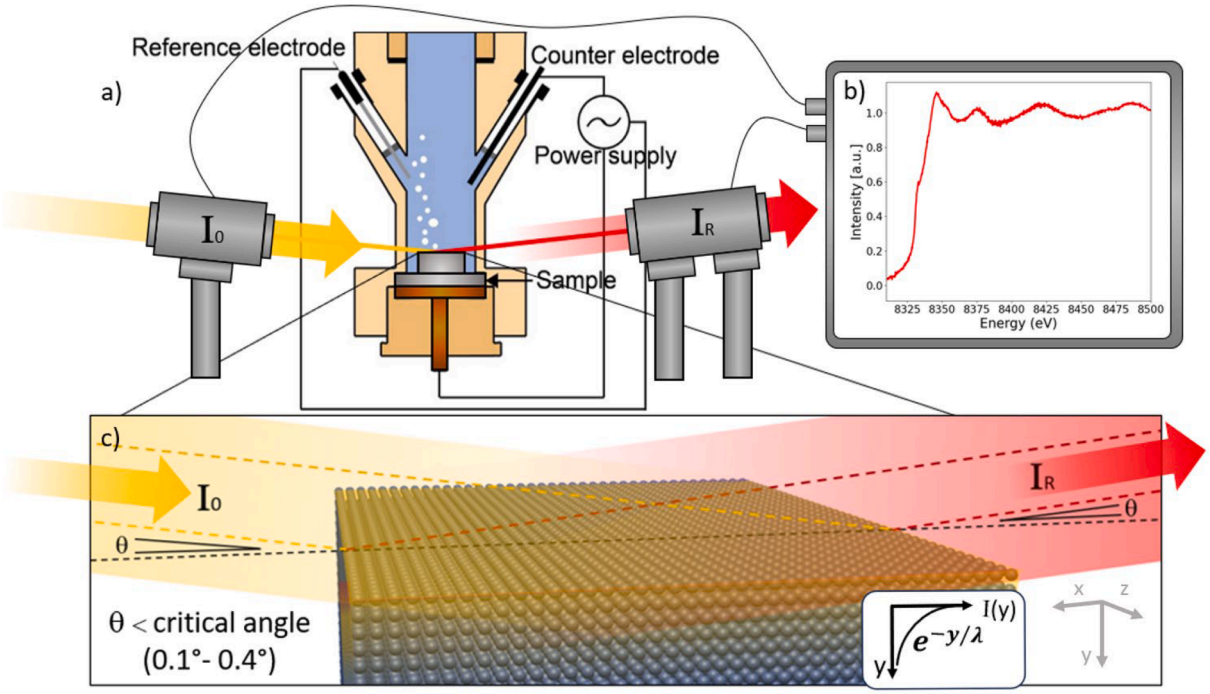

Fig. 1. (a) Schematic illustration of a Refle-XAFS configuration combined with the present EC flow cell. (b) Example of a normalized Refle-XAFS spectrum at the Ni K-edge (8331.5 eV) measured in this experiment. (c) Schematic illustration of the TER principle, I_0 corresponds to the incident beam, I_R to the totally reflected beam and θ to the incident angle.

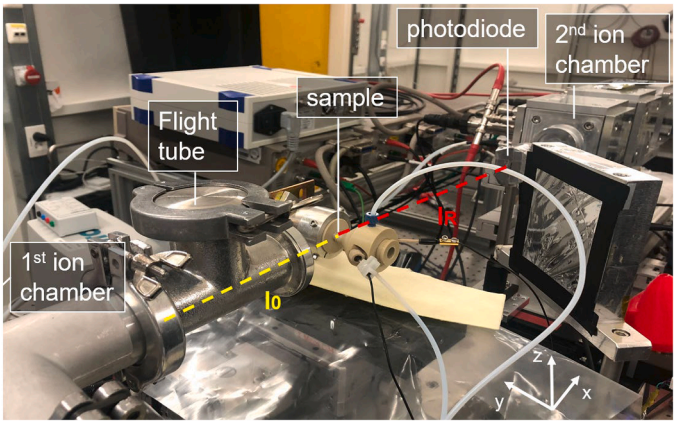

Fig. 2. *Operando* Refle-XAFS configuration setup at the P64 beamline at PETRA III, DESY, Hamburg. I_0 indicates the incident X-ray beam, while I_R indicates the reflected beam; the spatial reference system adopted is the same used in Fig. 1.

substrate at the interface with vacuum, pure H_2O and pure H_2SO_4, using the Center of X-ray Optics (CXRO) database [64]. A table of the calculated critical angle values is shown in supplementary information (Table S4). Accordingly, the incident angle was set below the lowest critical angle of the metal substrate (Au or Ni) depending on the absorption edge energy to be measured. As a result, the poly-Au studies were performed at ~0.2° (~3.5 mrad) incident angle, while for the Ni alloy 59 samples angels of ~0.1° (~1.7 mrad) for Mo K-edge and ~0.2° (~3.5 mrad) for Ni K-edge were used, respectively.

The reflected beam was measured with a photodiode (PD) placed 30 cm away from the sample along the reflected beam path. The PD was covered with strips of lead foil to produce a 1 mm slit defining the detector acceptance. The TER position for the PD was found after sample alignment, by scanning the PD and measuring the intensity along the y-direction to find the first maximum close to the direct beam, corresponding to the totally reflected beam, as shown in supplementary information (Fig. S3).

The incident beam intensity was measured with an ion-chamber placed upstream from the EC cell (Fig. 2). A second ion-chamber was placed downstream from the PD along the direct beam direction (Fig. 2) and was only used to measure spectra in transmission mode from foils or pellets of known compounds used as references. The gas composition of both ion chambers was set to 100 % N_2 to measure the Ni K-edge, 10 % Kr - 90 % N_2 for the Mo K-edge, and 10 % Ar - 90 % N_2 for the Au L_3-edge, with a total pressure of 1050 mbar. Refle-XAFS spectra were acquired while a constant polarization was applied and with static electrolyte, which was refreshed at each potential step before starting the measurements. Several scans, 120 s long, were recorded and averaged, with typical total measurement times of 6 min. EC measurements were performed using an Autolab PGSTAT101 potentiostat. A Pt rod was used as counter electrode and an eDAQ ET072–1 leakless miniature Ag/AgCl as reference electrode (RE). The miniature RE was first calibrated with respect to a standard Ag/AgCl RE showing a shift of -5 mV.

The EC cell, tubing and glassware were cleaned with 30 % HNO_3 followed by rinsing with ultrapure Milli-Q (mQ) water (18.2 MΩ). The Ni alloy 59 sample was sonicated in acetone for 15 min and then rinsed with mQ water. *Operando* measurements were performed in a 1 M NaCl electrolyte at pH 7 and adding NaOH to adjust the pH for electrolyte at pH 12. At each pH, two Ni alloy 59 samples were used: one to measure the Mo K-edge and one for Ni K-edge. Spectra were measured from the Open Circuit Potential (OCP) to above passivity breakdown with potential steps of 100 mV. Before performing Refle-XAFS measurements on the Ni alloys, a constant electrochemical polarization was applied for 10 min while recording the current with the beam shutter closed, then the shutter was removed and Refle-XAFS measurements were performed, while EC potential was still applied.

Reference spectra were measured in transmission-mode from pellets of pure oxide and hydroxide compounds powders, the pellets were prepared using cellulose as binder in the DESY chemistry lab. Pure metals foils were provided by the beamline staff, and Ni-Cr-Mo alloy foils were purchased from Goodfellow (UK). Depending on the

concentration of the element in the alloy foils and on the absorption edge energy of the investigated element, different thicknesses were used. Based on the commercial availability of thin alloy foils with similar composition to Ni alloy 59, a 10 μm foil of Hastelloy-B was used for the Ni K-edge and a 50 μm foil of Inconel 625 was used for the Mo K-edge. The Ni alloy foils compositions are specified in supplementary information (Table S5).

The poly-Au sample was cleaned with 3 cycles of the following stripping procedure: electro-oxidation at 10 V (0.2–0.3 Acm^{-2}) in 0.1 M H_2SO_4 with a graphite counter electrode for 20 s followed by dipping in HCl with no EC potential applied for 3 min. The last stripping cycle was followed by flame annealing with a butane torch and subsequent cooling in an N_2 atmosphere. The electrolyte was purged with Ar bubbling for an hour before the experiment. Au L_3-edge absorption spectra were measured in *operando* conditions at OCP and from 1500 mV to 2200 mV vs Ag/AgCl with 100 mV potential steps in a 0.05 M H_2SO_4 solution. At each potential step, before measuring Refle-XAFS spectra, fresh electrolyte was flown in the cell and Cyclic Voltammetry (CV) from -100 mV vs Ag/AgCl up to the potential step value was measured and then the current was recorded under constant EC polarization while the shutter was closed waiting for the current to stabilize for 5 min, without exposing the sample to the X-rays. Then the shutter was removed and Refle-XAFS measurements were performed, while EC potential was still applied.

Refle-XAFS data processing was performed using the Athena package [55]. The absorption-like data shown in the results and discussion section were processed first by taking the logarithm of the ratio of I_0 to I_R. Then, a linear background line was regressed to the data in the pre-edge

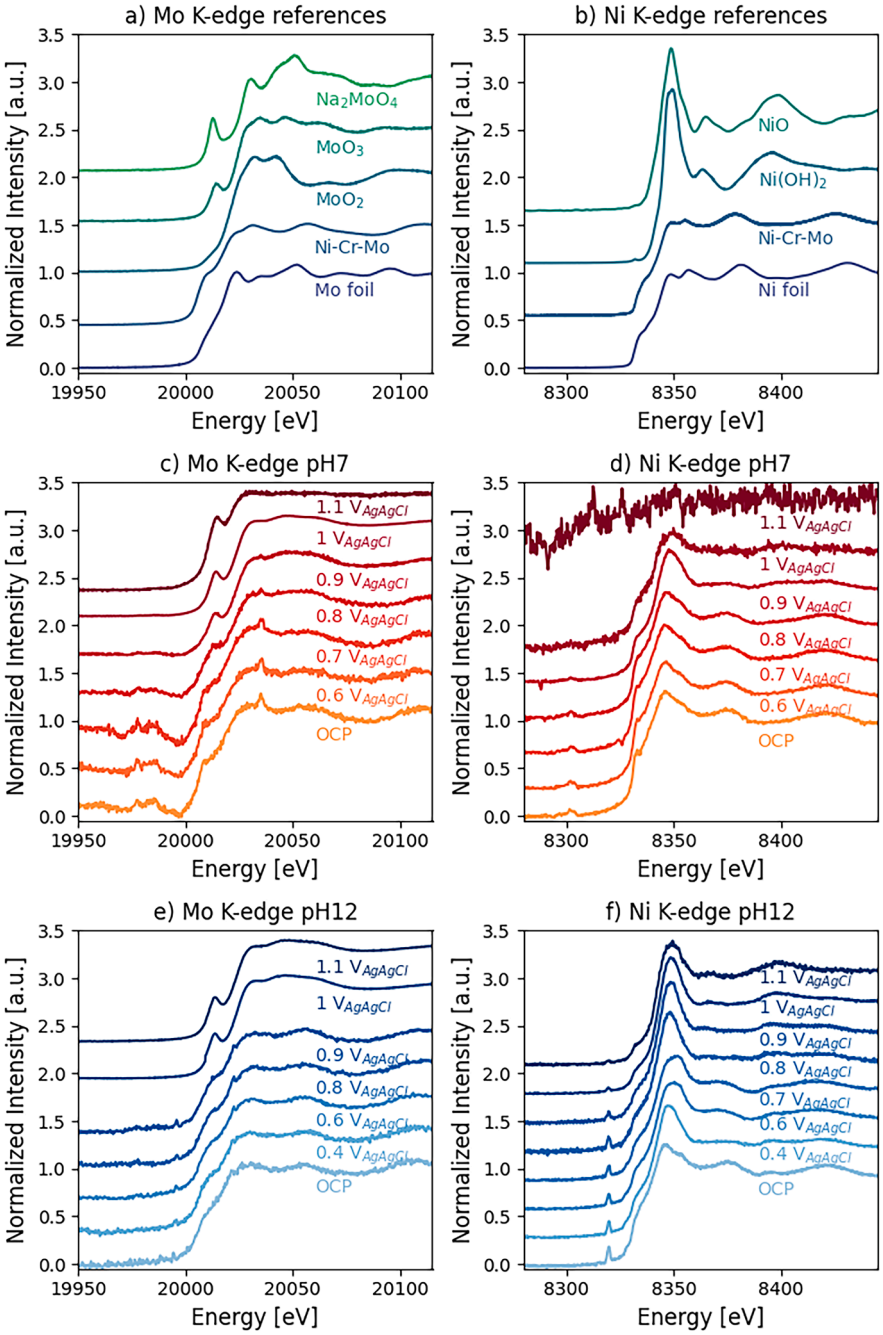

Fig. 3. (a) Mo and (b) Ni K-edges reference spectra measured in transmission mode. (c) and (d) Mo and Ni K-edges measured in total reflection geometry at pH 7 from Ni Alloy 59. (e) and (f) Mo and Ni K-edges measured in total reflection geometry at pH 12 from Ni Alloy 59.

region and a second-order polynomial was regressed to the data in the post-edge region. Finally, the absorption edge-step was set to 1. The raw data I_R/I_0 are shown in Fig. S8.

3. Results and discussion

3.1. Ni alloy 59 passivity breakdown

In the first part we explore the application of *operando* Refle-XAFS to corrosion studies of industrial alloys, using Ni alloy 59 as an example, which we have previously studied extensively in neutral and acidic electrolytes [9,16,65,66]. Corrosion resistant alloys are characterized by the spontaneous formation of a nm-thin oxide film, referred to as passive film, that protects the surface from corrosion [16,65,66]. It is well known that at high anodic polarization, passivity breakdown occurs, concurrently with a strong increase of the measured current, while a corrosion product film can form on the surface [9,25]. The effects of these features on the measurements will be discussed. Furthermore, passivity breakdown behavior at pH 12 will be explored and compared to the well-studied behavior at pH 7, relevant to understand the effect of pH on the complex interplay between electrocatalytic activity, stability and corrosion resistance of Ni-Cr-Mo alloys during OER.

All the EC potential values reported in this section are expressed on the Ag/AgCl scale. Fig. 3 summarizes the results of the experiment, showing normalized transmission mode X-ray absorption near edge spectroscopy (XANES) and Refle-XAFS spectra at the Ni and Mo K-edges. Transmission-mode and Refle-XAFS mode spectra are not entirely comparable, due to different normalization parameters used and artifacts introduced by reflection and scattering phenomena [45]. A qualitative analysis can be done by observing intensities and energies of pre-edge and near-edge features of the spectra [40]. Intensity changes of these features are highlighted in the difference-XANES and difference-Refle-XAFS spectra (Fig. S3), where the initial spectra measured at OCP are subtracted from the subsequent spectra measured at constant anodic polarization.

Fig. 3a and b show reference XANES spectra at the Ni and Mo K-edges, measured in transmission mode. Oxide and hydroxide reference compounds were chosen based on previous observations on Ni alloy 59 samples with XPS [16,65]. In Fig. 3a around 20,009 eV at the Mo K-edge, the Ni-Cr-Mo alloy foil exhibits a more pronounced pre-edge shoulder than that of pure metallic Mo. For the Ni K-edge spectra in Fig. 3b both pure metallic Ni and the Ni-Cr-Mo alloy foil exhibit a pronounced pre-edge shoulder around 8334 eV. The absence of the pre-edge shoulder for metallic Mo, is attributed to the fact that metallic Mo has a body-centered-cubic lattice (BCC), whilst metallic Ni and Ni-Cr-Mo alloy have a face-centered-cubic (FCC) structure [67]. From the Mo K-edge reference compounds spectra in Fig. 3a is possible to distinguish Mo^{3+} from Mo^{6+} oxides by looking at the presence of a distinct pre-edge peak around 20,013 eV, which shows up only in the case of Mo^{6+} compounds. Furthermore, Na_2MoO_4 shows a peak around 20,050 eV that can be used to distinguish it from MoO_3. In Fig. 3b Ni^{2+} oxides/hydroxides compounds exhibit a strong absorption white-line around 8346 eV, which is absent in case of metallic reference spectra. These features will be the main distinguishers in the qualitative analysis of the following Refle-XAFS spectra.

Fig. 3c and d show Refle-XAFS measurements at pH 7 at the Ni and Mo K-edges. The pre-edge shoulders observed in Fig. 3a and b for metallic FCC structures at the Mo K-edge around 20,009 eV and at the Ni K-edge around 8334 eV are also observed for both K-edges at OCP in Fig. 3c and d, respectively. The presence of oxide components at OCP is not directly evident from these spectra, suggesting that there are only small amounts of Mo and Ni oxides/hydroxides compounds in the passive film. This is in agreement with previous XPS and AP-XPS studies on the composition of the passive film of Ni alloy 59, showing a dominant Cr^{3+} oxide content [9,16,65,66]. From measurements at increasing EC potential in Fig. 3c and d, we observe significant changes in the spectra from 0.8 V, attributed to passivity breakdown. In particular, a distinct pre-edge peak at 0.8 V starts appearing around 20,009 eV at the Mo K-edge (Fig. 3c) and the white line at the Ni K-edge grows in intensity around 8346 eV (Fig. 3d). These peaks correlate with the formation of Mo^{6+} and Ni^{2+} compounds, as seen by comparison with the reference spectra in Fig. 3a and b. The absence of a peak at 20,050 eV at the Mo K-edge in Fig. 3c suggests that MoO_3 is the main component observed. Above 0.8 V, the contribution of Ni and Mo oxides/hydroxides components grows significantly, suggesting a formation of corrosion products on the surface as passivity breakdown occurred, in agreement with the AP-XPS results [9]. At 1.1 V in Fig. 3c and at 1 V in Fig. 3d the signal-to-noise ratio starts decreasing and the intensity oscillations above the absorption edges are much weaker. Furthermore, the Ni K-edge signal disappears completely at 1.1 V, suggesting a low amount of Ni compounds present in the corrosion products at high anodic polarization. The overall decrease in the total reflected intensity is attributed to significant roughening of the surface, as discussed in the supplementary information (Fig. S4) together with an interpretation about how the absorption steps are affected by roughness.

Fig. 3e and f show Refle-XAFS measurements at pH 12 at the Ni and Mo K-edges. At OCP in Fig. 3e and f, we observe the same spectra measured at pH 7 (Fig. 3c and d). However, with increasing EC potential the behavior at pH 12 appears different from that observed at pH 7, especially at the Ni K-edge (Fig. 3f). In Fig. 3f changes in the spectra can be observed already at 0.4 V, where the white line intensity around 8346 eV increases significantly with respect to OCP. Furthermore, spectra observed at 0.6 V and 0.7 V in Fig. 3f exhibit a peak around 8353 eV which does not correspond to either of the measured Ni^{2+} reference compounds (Fig. 1b). This peak has been commonly observed for NiOOH in other XAS studies [68,69] and the EC potential range where we observe this peak is compatible with that of $Ni(OH)_2$ to NiOOH transition, where Ni^{2+} can be further oxidized to Ni^{3+} [69–71]. However, above 0.7 V in Fig. 1b the peak around 8353 eV associated to the NiOOH component is not visible anymore, while the white line intensity around 8346 eV keeps growing, indicating the growth of $NiO/Ni(OH)_2$ on the surface. For the Mo K-edge at pH 12 (Fig. 3e) we observe an abrupt appearance at 1 V of the pre-edge peak around 20,009 eV, characteristic of Mo^{6+} compounds. The absence of a peak around 20,050 eV at the Mo K-edge in Fig. 3e again suggests the formation of mainly MoO_3.

The trends of the main components observed with increasing EC potential at pH 12 and 7 are highlighted and compared using linear combination fitting (LCF), making use of spectra at low and high EC potentials as internal standards. Specifically, we used the OCP spectra and 1.1 V spectra measured at pH 12 for the Mo K-edges and the OCP spectra and 1 V spectra measured at pH 12 for the Ni K-edges. The results are plotted in Fig. 4 together with the steady-state current values measured after 10 min under constant EC polarization.

Fig. 4a shows steady-state current values measured after 10 min at constant EC potential for pH 7 and 12. At pH 7, the abrupt current increase after 0.8 V observed in Fig. 4a takes place at the same EC potential at which we observe a significant increase of MoO_3 (Fig. 4b) and $NiO/Ni(OH)_2$ (Fig. 4c), where passivity breakdown and OER are expected to take place [9].

At pH 12 in Fig. 4a the current increases already at 0.7 V, but up to 0.9 V is not exponentially increasing and concurrently the $Ni(OH)_2$ to NiOOH transition is observed in Fig. 3f. The temporary presence of NiOOH is not taken into account in the LCF since the internal standards do not contain NiOOH, indeed a larger discrepancy in the fitting is observed at 0.6 V and 0.7 V, e.g. in Fig. S9. An exponential increase of the current at pH 12 is observed only from 1 V, when MoO_3 is suddenly detected (Fig. 4b). The overall higher amount of Ni^{2+} compounds observed for the entire experiment at pH 12 with respect to pH 7 is highlighted in Fig. 4c.

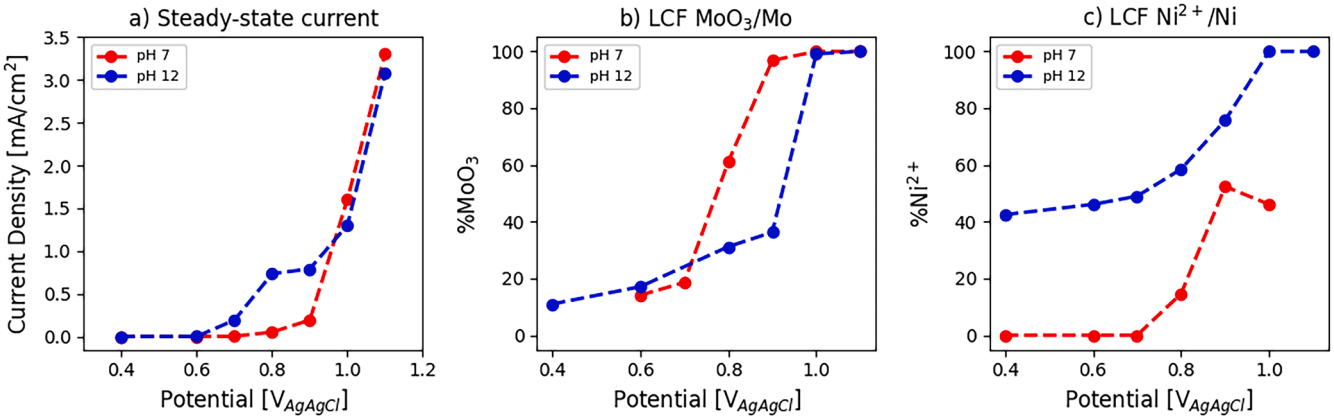

Fig. 4. (a) Steady-state current measured after 10 min at constant EC potential for Ni alloy 59 at pH 7 and pH 12. (B) and (c) LCF for MoO_3/Mo and Ni^{2+}/Ni at increasing EC potential.

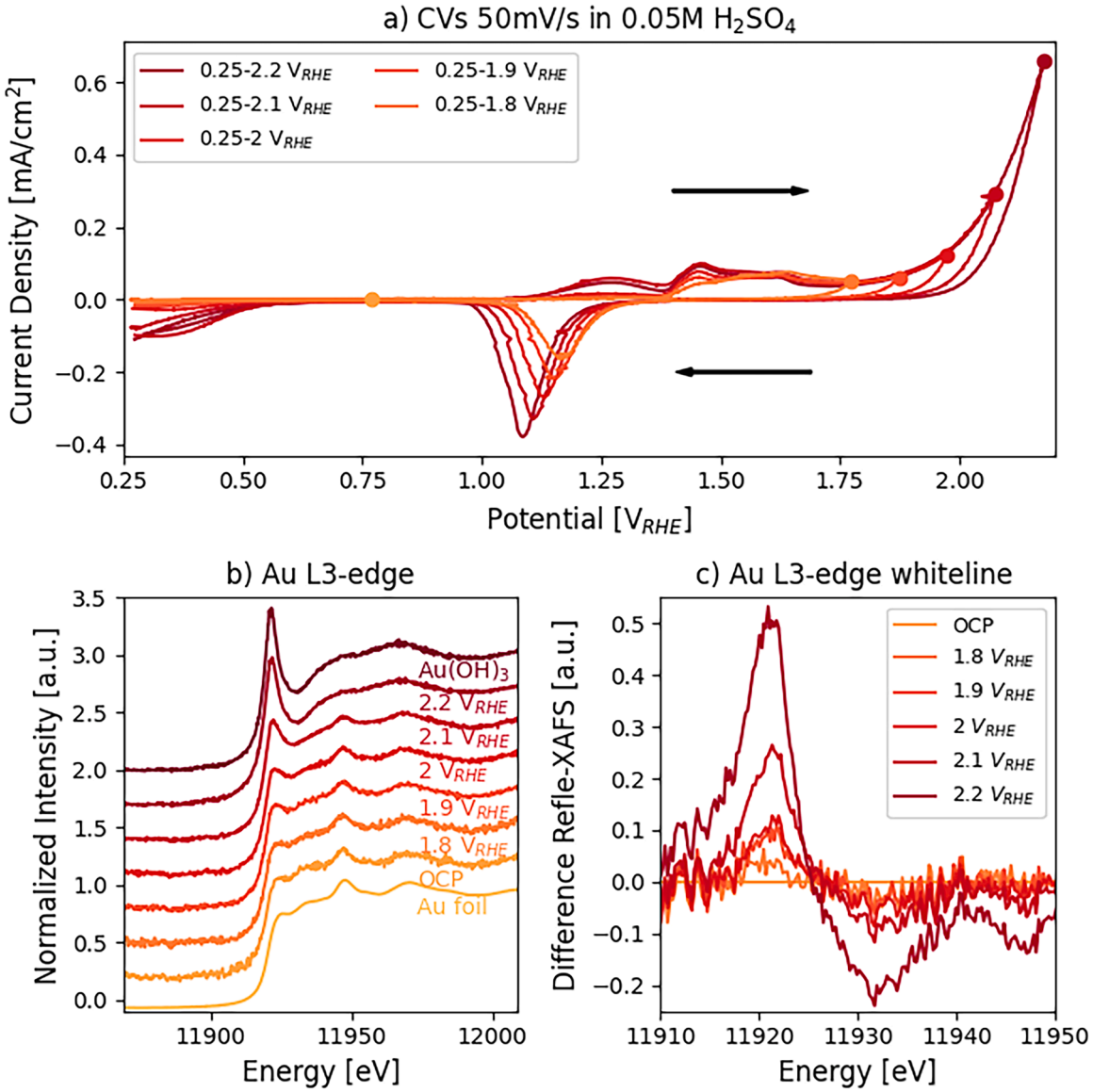

Fig. 5. (a) CVs from 0.25 V to increasing upper vertex potentials. Colored dots correspond to the constant potential at which Refle-XAFS were measured. (b) Au L3-Edge XANES from reference Au foil and $Au(OH)_3$ measured in transmission mode, and *operando* Refle-XAFS from poly-Au in 0.05 M H_2SO_4 (c) Difference-Refle-XAFS at each EC potential with respect to OCP.

3.2. Au electro-oxidation

In this section we apply Refle-XAFS to a poly-Au electrode as a model system to study the electro-oxidation of Au surfaces [17,59–61]. Such surfaces have been studied previously by *in situ* high energy surface XRD (HESXRD) and SOR [18], and though it is believed that gold oxides/hydroxides form on these surfaces under OER conditions, these compounds appear to be amorphous and so are not reflected in the XRD signals. Previous studies have correlated Au^{3+} to thick Au-oxides/hydroxides formed in OER [7,59,72], whilst it is still under debate if Au^{3+} or Au^{1+} species are formed before OER [7,17,73].

All the EC potential values reported in this section are expressed on the reversible hydrogen electrode (RHE) scale. Fig. 5 summarizes the results of the experiment. Fig. 5a shows CVs at increasing upper potentials for poly-Au in 0.05 M H_2SO_4. During the forward (anodic) sweeps in the CVs, between 1.4 V and 1.75 V, the so-called oxidation peaks are present (1), associated to at least a partial oxidation of the surface atoms of different grains [7,17,18,59,60]. The subsequent exponential increase of the current at higher EC potentials is associated with the onset of OER (2), i.e. H_2O splitting, which could be accompanied by dissolution and oxidation of the electrode surface [7,17,18,59,60]. From a pure EC point of view, the oxide thickness correlates to the increase and shift of the reduction peak (3) between 1.25 V and 1 V during the backward (cathodic) sweep, where a more negative EC potential is needed to fully reduce a thicker oxide/hydroxide to metallic Au [7,17,18,59,60]. Hence, the increasing shift to lower EC potentials observed in the reduction peak for increasing upper EC potential applied suggests the further growth of a thicker oxide onto the surface during OER. Furthermore, when significant OER current is measured, i.e. for upper EC potentials above 2 V, new voltammetric features are observed below 0.5 V (4) in the cathodic sweep and around 1.25 V (5) in the anodic sweep. The cathodic current measured below 0.5 V (4) can be correlated to the oxygen reduction reaction (ORR): even after refreshing the electrolyte, a small amount of generated oxygen remained dissolved in the electrolyte due to OER, resulting in ORR cathodic current measured below 0.5 V (4) [74]. The ORR on Au has commonly been associated with the reduction of O_2 to both H_2O and H_2O_2, the former reaction has a thermodynamic EC potential (E_0) of 1.23 V and the latter of 0.67 V [74]. Together with increasing ORR measured current, an anodic current peak grows around 1.25 V (5) in the subsequent forward sweeps, which is attributed to the splitting of H_2O_2 which was formed during ORR [74].

Fig. 5b shows transmission mode XANES of $Au(OH)_3$ and Au references together with Refle-XAFS spectra measured at constant EC potential. A nominal Au_2O_3 reference was also measured, but this showed a spectrum identical to that of $Au(OH)_3$, which we suspect is due to hydration of the Au_2O_3 from exposure to air, since Au_2O_3 is not thermodynamically stable in these conditions [7]. The most obvious change of the Au spectra is the increase in the white line around 11,919 eV, as the EC potential is increasing. Investigations on the actual Au L3-edge XANES for different oxidation states of gold have not identified a significant contributions to the white line from pure Au^{1+} compounds [75]. A large white line increase should be proportional to the density of unoccupied 5d states, which increases with increasing Au^{3+}/Au ratio [76,77]. Such changes are highlighted in Fig. 5c, where the spectrum corresponding to OCP has been subtracted to each of the spectra measured at different EC potentials. From Fig. 5c is possible to observe a small increase in the white line already at 1.8 V, indicating the presence of a small, oxidized component. At 2.2 V, the white line intensity is significantly higher, and the spectrum in Fig. 5b resembles that of reference $Au(OH)_3$.

Fig. 6 summarizes the trends observed in the measurements. Fig. 6a shows an exponential increase of the steady-state current after 2 V, which is partially associated to a significant amount of OER occurring. LCF (Fig. 6b) was performed using the OCP spectrum and $Au(OH)_3$ reference spectrum, showing a significantly steeper increase of hydroxide signal above 2 V, when current increases exponentially. For an ideally perfectly flat surface, the volume of the probed (absorbing) material can be estimated using the penetration depth of the evanescent wave into the material along the surface normal. At energies in the white line region of the Au L3-edge, where LCF was calculated, the penetration depth at 0.2° incident angle is between 1.8 and 1.9 nm, according to CXRO database [64]. This suggests that~ 63 % of the signal comes from an absorbing volume with less than 2 nm thickness. Therefore, this is the order of magnitude of the hydroxide thickness growing at high EC potentials during OER, and only monolayers thicknesses at the initial stages when the LCF shows less than 20 % of $Au(OH)_3$, before OER. Fig. 6c shows the measured specular reflectance signal intensity and the absorption step size as a function of EC potential. The specular reflectance signal intensity did not show significant changes during the experiment. However, at 2.2 V, an increase in the absorption step size and a small decrease in reflectance signal are observed. As discussed in supplementary information (Fig. S4), the absorption step size is proportional to the amount of absorbing material in the beam path, while the reflectance is affected by surface roughness and refractive index. When the Au -oxides or -hydroxides grow on the surface, the density of absorbing atoms is lower than the pure Au metal, then the absorption step size should in principle slightly decrease. It is proposed that what could cause the increase in the absorption step size at high EC potential is the surface morphology [42,43]: as the surface roughens, some photons

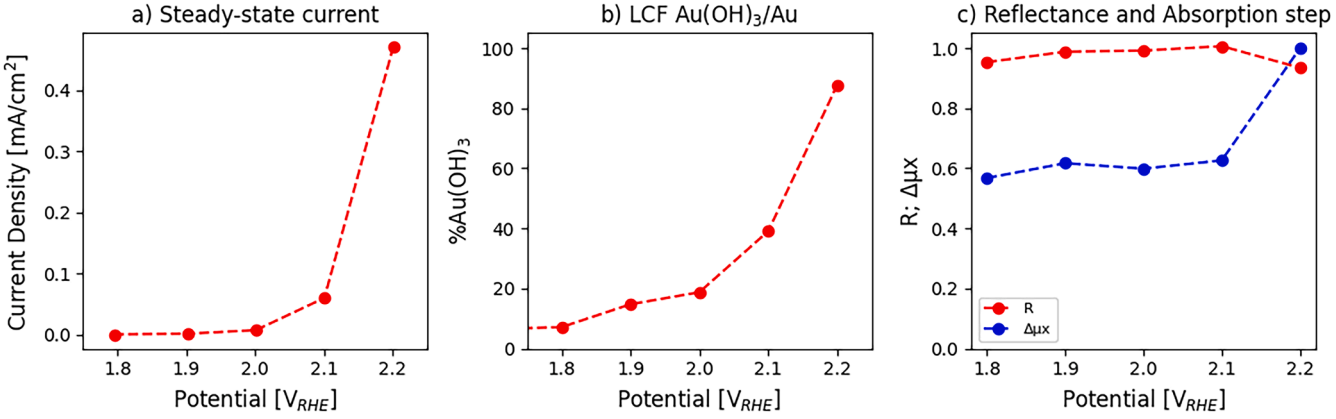

Fig. 6. (a) Steady-state current values measured after 5 min at constant applied EC potential. (b) LCF of operando Refle-XAFS spectra using the Refle-XAFS spectrum at OCP and the transmission mode XANES spectrum of $Au(OH)_3$ as references. (c) Specular reflectance signal intensity (red) measured at 11,820 eV calculated as the ratio between the reflected (I_R) and incident beam (I_0) intensity and normalized to the highest value of reflectance measured in the experiment. Absorption step size (blue) measured at the Au L3-edge (11,919 eV) and normalized to the highest absorption step size measured in the experiment.

can be transmitted through islands, clusters and other 3D-defects forming on the surface. In this case, the transmission through defects contributes to the total volume of absorbing material probed by the beam, which can increase the absorption step size. Roughening may also lead to a reduced signal of the near surface species and an enhanced bulk signal [42,43], but the large increase in the Au L3-edge white line intensity associated to an increased amount of Au^{3+} clearly shows that further oxidation is taking place. Thus, the decrease in specular reflectance signal intensity and the increase in absorption step size may indicate that a larger volume of absorbing material is probed, associated to the presence of 3D hydroxide islands growing on the surface at high EC potentials.

Measurements were performed also above 2.2 V, however under these conditions an anomalous behavior was observed that we associate with beam damage. In particular, reducing white line intensities were observed during successive Refle-XAFS scans, which we attribute to formation and beam-induced reduction of a thick and unstable hydroxide [78]. In fact, moving the sample across the beam, thus illuminating a new sample region, resulted in the reappearance of the hydroxide signal. These spectra are plotted in Fig. S5 in supplementary information. Sample beam damage produced a visible black stripe across the sample, which was also investigated with SEM, see Fig. S6 in the supplementary information.

3.3. Setup evaluation

To validate the use of Refle-XAFS, the measurements were performed also in fluorescence mode for both the case studies, where a higher signal-to-noise ratio was measured but no changes in the fluorescence spectra were observed with increasing EC potential. As an example, Ni K-edge spectra measured *operando* at pH 12 in fluorescence mode in TER geometry are shown in supplementary information (Fig. S7), highlighting that all the spectra are mostly equal to the bulk metallic Ni spectrum. In fact, TER could also in principle be exploited in fluorescence mode to study surfaces of thick samples, but it is rather difficult to avoid the incident beam impinging also on sample edges and on macroscopic defects, significantly lowering the surface sensitivity. Refle-XAFS instead is an inherently surface sensitive technique, as the detected totally reflected beam is the part of the beam that interacts only with the surface region. In fact, though the beam size used in this experiment leads to a beam footprint larger than the sample, these measurements show that useful information is contained in the detected signal. There is however a risk of artifacts and incomplete compensation for variations in the photon flux, making e.g. the extended fine structure analysis hazardous or impossible, but such effects are small enough that useful near-edge spectra are nevertheless acquired.

AP-XPS studies on Ni alloy 59 have shown a higher sensitivity to small changes in the passive film composition after anodic polarization [16]. In fact, despite the passivity breakdown, the detection of corrosion products using Refle-XAFS is slightly delayed with respect to AP-XPS [9], suggesting a comparable but lower surface sensitivity of Refle-XAFS. However, a lower surface sensitivity can be beneficial when thicker films are grown on a substrate, or to study the subsurface region of the sample.

Surface sensitivity is determined by the penetration depth of the evanescent wave, so it is a function of the sample refractive index, beam energy and incident angle, which are almost fixed. What can be improved is the signal-to-noise ratio from the surface, for example by optimizing the beam focus to maximize the number of photons reflecting on the surface. Furthermore, in the ideal case that the entire beam is focused enough to have a footprint smaller than the sample size, a reduced diameter of the EC cell could be produced to reduce the beam path across the electrolyte, and consequently the beam attenuation. This would in principle open possibilities to detect lower concentrations of species, to measure at lower absorption edge energies, and to measure the small oscillations in the extended X-ray absorption fine structure (EXAFS) region. However, a more focused beam requires high stability during the energy scans. In case there are inhomogeneities or not flat surfaces, beam instabilities can induce artifacts in the measurements, as the probed sample region can change significantly. Hence, a careful consideration of the concentration of surface species and beam attenuation needs to be done according to the samples to be studied and the beamline capabilities.

Beyond the possibility to use Refle-XAFS, this EC cell design shows also other advantages. First of all, the use of a bulk (mL_s volume) electrolyte configuration allows to perform experiments in a more reproducible and scalable manner, and with the possibility to accommodate large bubbles in the EC cell developed during OER without any issue. Moreover, if species dissolve in the electrolyte, hard X-ray spectroscopy techniques can be used to investigate the nature of dissolved species by moving the beam above the surface, even by several mm_s. Furthermore, the cell allows 360° rotation using cylindrical samples, which is very important, e.g., in the case of HESXRD measurements, where the samples usually need to be rotated in a wide angular range. Another relevant advantage is that the cell can accommodate large scattering angles, important for example in the case of wide-angle X-ray scattering (WAXS) and X-ray reflectivity (XRR) experiments.

4. Conclusions

By using Refle-XAFS in *operando* conditions, we have investigated the passivity breakdown of the industrial Ni alloy 59 and the electro-oxidation of a poly-Au sample under stepwise increasing EC anodic polarization. We have shown that our set-up is suitable for energies as low as 8 keV, providing sub-nanometer surface sensitivity in real *operando* conditions. Reflectance signal intensity below the absorption edge and absorption step size were correlated to changes in surface morphology and composition.

The Ni alloy 59 corrosion studies show a similar passivity breakdown potential as previous studies at pH 7 [9,16], identifying MoO_3 as the main corrosion product forming in conjunction with the observation of an exponential increase of the steady-state current. At this pH, only low amount of Ni oxidizes to $NiO/Ni(OH)_2$ at the passivity breakdown potential. At pH 12 instead, $NiO/Ni(OH)_2$ are observed on the surface at lower EC potentials and in larger amounts, until passivity breakdown occurs, while MoO_3 forms as main corrosion product at higher EC potentials with respect to pH 7.

Poly-Au electro-oxidation was also studied indicating the formation of a thin 2D-(hydro)oxide at the oxidation peak, and the formation of a thicker $3D\text{-}Au_2O_3/Au(OH)_3$ during the OER. Reduction of the Au^{3+} signal was observed at high EC potentials, which we attribute to the beam-induced reduction of a thick and unstable hydroxide.

CRediT authorship contribution statement

A. Grespi: Writing – review & editing, Writing – original draft, Visualization, Methodology, Investigation, Formal analysis, Data curation, Conceptualization. **A. Larsson:** Writing – review & editing, Methodology, Investigation, Formal analysis, Conceptualization. **G. Abbondanza:** Writing – review & editing, Investigation. **J. Eidhagen:** Writing – review & editing, Investigation. **D. Gajdek:** Methodology, Investigation. **J. Manidi:** Writing – review & editing, Investigation. **A. Tayal:** Methodology, Investigation. **J. Pan:** Writing – review & editing, Validation, Resources, Funding acquisition, Formal analysis. **L.R. Merte:** Writing – review & editing, Validation, Supervision, Resources, Methodology, Investigation, Funding acquisition, Formal analysis, Conceptualization. **E. Lundgren:** Writing – review & editing, Validation, Supervision, Resources, Methodology, Funding acquisition, Conceptualization.

Declaration of competing interest

The authors declare that they have no known competing financial interests or personal relationships that could have appeared to influence the work reported in this paper.

Data availability

Data will be made available on request.

Acknowledgments

Financial support was acknowledged from the Swedish Research Council (2018–03434 and 2020–06154) and the Swedish Foundation for Strategic Research under contract ID19–0032. The authors acknowledge DESY (Hamburg, Germany), a member of the Helmholtz Association HGF, for the provision of experimental facilities. This research was carried out at PETRA III, and the authors would like to thank Wolfgang Caliebe, Aleksandr Kalinko, Maria Naumova and Claudia Schwan for assistance in using the Advanced XAFS beamline P64, and Milena Lippmann for assistance with the chemistry laboratories at DESY. Beamtime at DESY was allocated for the proposal I-20211350 EC and I-20221038 EC.

Supplementary materials

Supplementary material associated with this article can be found, in the online version, at doi:10.1016/j.susc.2024.122538.

References

[1] D.D. Macdonald, Passivity–the key to our metals-based civilization, Pure Appl. Chem. 71 (6) (1999) 951–978, https://doi.org/10.1351/pac199971060951.
[2] V. Maurice, P. Marcus, Current developments of nanoscale insight into corrosion protection by passive oxide films, Curr. Opin. Solid State Mater. Sci. 22 (4) (2018) 156–167, https://doi.org/10.1016/j.cossms.2018.05.004.
[3] N.T. Suen, S.F. Hung, Q. Quan, N. Zhang, Y.J. Xu, H.M. Chen, Electrocatalysis for the oxygen evolution reaction: recent development and future perspectives, Chem. Soc. Rev. 46 (2) (2017) 337–365, https://doi.org/10.1039/C6CS00328A.
[4] A. Ursua, L.M. Gandia, P. Sanchis, Hydrogen production from water electrolysis: current status and future trends, in: Proceedings of the IEEE 100, 2012, pp. 410–426, https://doi.org/10.1109/JPROC.2011.2156750. Feb.
[5] P. Simon, Y. Gogotsi, Perspectives for electrochemical capacitors and related devices, Nat. Mater. 19 (11) (2020) 1151–1163, https://doi.org/10.1038/s41563-020-0747-z.
[6] Z. Yang, J. Zhang, M.C.W. Kintner-Meyer, X. Lu, D. Choi, J.P. Lemmon, J. Liu, Electrochemical energy storage for green grid, Chem. Rev. 111 (5) (2011) 3577–3613, https://doi.org/10.1021/cr100290v.
[7] O. Diaz-Morales, F. Calle-Vallejo, C. De Munck, M.T.M. Koper, Electrochemical water splitting by gold: evidence for an oxide decomposition mechanism, Chem. Sci. 4 (6) (2013) 2334, https://doi.org/10.1039/c3sc50301a.
[8] F. Zeng, C. Mebrahtu, L. Liao, A.K. Beine, R. Palkovits, Stability and deactivation of OER electrocatalysts: a review, J. Energy Chem. 69 (2022) 301–329, https://doi.org/10.1016/j.jechem.2022.01.025.
[9] A. Larsson, A. Grespi, G. Abbondanza, J. Eidhagen, D. Gajdek, K. Simonov, X. Yue, U. Lienert, Z. Hegedüs, A. Jeromin, T.F. Keller, M. Scardamaglia, A. Shavorskiy, L. R. Merte, J. Pan, E. Lundgren, The oxygen evolution reaction drives passivity breakdown for Ni–Cr–Mo alloys, Adv. Mater. (2023) 2304621, https://doi.org/10.1002/adma.202304621.
[10] P. Marcus, Surface science approach of corrosion phenomena, Electrochim. Acta 43 (1–2) (1998) 109–118, https://doi.org/10.1016/S0013-4686(97)00239-9.
[11] A. Cuesta, M. Kleinert, D.M. Kolb, The Adsorption of sulfate and phosphate on Au (111) and Au(100) electrodes: an *in situ* STM study, Phys. Chem. Chem. Phys. 2 (24) (2000) 5684–5690, https://doi.org/10.1039/b006464p.
[12] A.D. Handoko, F. Wei, Jenndy, B.S. Yeo, Z.W Seh, Understanding heterogeneous electrocatalytic carbon dioxide reduction through operando techniques, Nat. Catal. 1 (12) (2018) 922–934, https://doi.org/10.1038/s41929-018-0182-6.
[13] S.Z. Oener, A. Bergmann, B.R Cuenya, Designing active oxides for a durable oxygen evolution reaction, Nat. Synth. 2 (2023) 817–827, https://doi.org/10.1038/S44160-023-00376-6.
[14] J.J. Velasco-Vélez, L.J. Falling, D. Bernsmeier, M.J. Sear, P.C.J. Clark, T.S. Chan, E. Stotz, M. Hävecker, R. Kraehnert, A. Knop-Gericke, C.H. Chuang, D.E. Starr, M. Favaro, R.V. Mom, A comparative study of electrochemical cells for *in situ* X-ray spectroscopies in the soft and tender X-ray range, J. Phys. Appl. Phys. 54 (12) (2021) 124003, https://doi.org/10.1088/1361-6463/abd2ed.
[15] S. Axnanda, E.J. Crumlin, B. Mao, S. Rani, R. Chang, P.G. Karlsson, M.O. M. Edwards, M. Lundqvist, R. Moberg, P. Ross, Z. Hussain, Z. Liu, Using "tender" X-ray ambient pressure X-ray photoelectron spectroscopy as a direct probe of solid-liquid interface, Sci. Rep. 5 (1) (2015) 9788, https://doi.org/10.1038/srep09788.
[16] A. Larsson, K. Simonov, J. Eidhagen, A. Grespi, X. Yue, H. Tang, A. Delblanc, M. Scardamaglia, A. Shavorskiy, J. Pan, E. Lundgren, *In situ* quantitative analysis of electrochemical oxide film development on metal surfaces using ambient pressure X-ray photoelectron spectroscopy: industrial alloys, Appl. Surf. Sci. 611 (2023) 155714, https://doi.org/10.1016/j.apsusc.2022.155714.
[17] C. Griesser, D. Winkler, T. Moser, L. Haug, M. Thaler, E. Portenkirchner, B. Klötzer, S. Diaz-Coello, E. Pastor, J. KunzeLiebhäuser, Lab-based electrochemical X-ray photoelectron spectroscopy for *in-situ* probing of redox processes at the electrified solid/liquid interface, Electrochem. Sci. Adv. (2023) e2300007, https://doi.org/10.1002/elsa.202300007.
[18] W. Linpé, L. Rämisch, G. Abbondanza, A. Larsson, S. Pfaff, L. Jacobse, J. Zetterberg, L. Merte, A. Stierle, Z. Hegedues, U. Lienert, E. Lundgren, G.S. Harlow, Revisiting optical reflectance from Au(111) electrode surfaces with combined high-energy surface X-ray diffraction, J. Electrochem. Soc. 168 (9) (2021) 096511, https://doi.org/10.1149/1945-7111/ac2702.
[19] T. Fuchs, V. Briega-Martos, J.O. Fehrs, C. Qiu, M. Mirolo, C. Yuan, S. Cherevko, J. Drnec, O.M. Magnussen, D.A. Harrington, Driving force of the initial step in electrochemical Pt(111) oxidation, J. Phys. Chem. Lett. 14 (14) (2023) 3589–3593, https://doi.org/10.1021/acs.jpclett.3c00520.
[20] J. Timoshenko, B. Roldan Cuenya, *In situ /Operando* electrocatalyst characterization by X-ray absorption spectroscopy, Chem. Rev. 121 (2) (2021) 882–961, https://doi.org/10.1021/acs.chemrev.0c00396.
[21] L.R. Merte, F. Behafarid, D.J. Miller, D. Friebel, S. Cho, F. Mbuga, D. Sokaras, R. Alonso-Mori, T.C. Weng, D. Nordlund, A. Nilsson, B. Roldan Cuenya, Electrochemical oxidation of size-selected Pt nanoparticles studied using *in situ* high-energy-resolution X-ray absorption spectroscopy, ACS Catal. 2 (11) (2012) 2371–2376, https://doi.org/10.1021/cs300494f.
[22] S.M. Gericke, J. Rissler, M. Bermeo, H. Wallander, H. Karlsson, L. Kollberg, M. Scardamaglia, R. Temperton, S. Zhu, K.G.V. Sigfridsson Clauss, C. Hulteberg, A. Shavorskiy, L.R. Merte, M.E. Messing, J. Zetterberg, S. Blomberg, *In situ* H2 reduction of Al2O3-supported Ni- and Mo-based catalysts, Catalysts 12 (7) (2022) 755, https://doi.org/10.3390/catal12070755.
[23] F.T. Haase, A. Bergmann, T.E. Jones, J. Timoshenko, A. Herzog, H.S. Jeon, C. Rettenmaier, B.R. Cuenya, Size effects and active state formation of cobalt oxide nanoparticles during the oxygen evolution reaction, Nat. Energy 7 (8) (2022) 765–773, https://doi.org/10.1038/s41560-022-01083-w.
[24] J. McBreen, S. Mukerjee, *In situ* X-ray absorption studies of a Pt-Ru electrocatalyst, J. Electrochem. Soc. 142 (10) (1995) 3399–3404, https://doi.org/10.1149/1.2049993.
[25] M. Långberg, C. Örnek, J. Evertsson, G.S. Harlow, W. Linpé, L. Rullik, F. Carlà, R. Felici, E. Bettini, U. Kivisäkk, E. Lundgren, J. Pan, Redefining passivity breakdown of super duplex stainless steel by electrochemical operando synchrotron near surface X-ray analyses, npj Mater. Degrad. 3 (1) (2019) 22, https://doi.org/10.1038/s41529-019-0084-3.
[26] G. Abbondanza, A. Grespi, A. Larsson, L. Glatthaar, T. Weber, M. Blankenburg, Z. Hegedüs, U. Lienert, H. Over, E. Lundgren, Anisotropic strain variations during the confined growth of Au nanowires, Appl. Phys. Lett. 122 (12) (2023) 123101, https://doi.org/10.1063/5.0138891.
[27] G. Abbondanza, A. Grespi, A. Larsson, D. Dzhigaev, L. Glatthaar, T. Weber, M. Blankenburg, Z. Hegedüs, U. Lienert, H. Over, G.S. Harlow, E. Lundgren, hydride formation and dynamic phase changes during template-assisted Pd electrodeposition, Nanotechnology (2023), https://doi.org/10.1088/1361-6528/acf66e.
[28] D. Gajdek, P.A.T. Olsson, S. Blomberg, J. Gustafson, P.A. Carlsson, D. Haase, E. Lundgren, L.R. Merte, Structural changes in monolayer cobalt oxides under ambient pressure CO and O_2 studied by *in situ* grazing-incidence X-ray absorption fine structure spectroscopy, J. Phys. Chem. C 126 (7) (2022) 3411–3418, https://doi.org/10.1021/acs.jpcc.1c10284.
[29] D. Friebel, D.J. Miller, D. Nordlund, H. Ogasawara, A. Nilsson, Degradation of bimetallic model electrocatalysts: an *in situ* X-ray absorption spectroscopy study, Angew. Chem. Int. Ed. 50 (43) (2011) 10190–10192, https://doi.org/10.1002/anie.201101620.
[30] D. Garai, A. Wilson, I. Carlomagno, C. Meneghini, F. Carla, H. Hussain, A. Gupta, J. Zegenhagen, Structure of the surface region of stainless steel: bulk and thin films, Phys. Status Solidi B 259 (4) (2022) 2100513, https://doi.org/10.1002/pssb.202100513.
[31] C. Maurizio, M. Rovezzi, F. Bardelli, H.G. Pais, F. D'Acapito, Setup for optimized grazing incidence X-ray absorption experiments on thin films on substrates, Rev. Sci. Instrum. 80 (6) (2009) 063904, https://doi.org/10.1063/1.3155791.
[32] S. Virtanen, *In situ* X-ray absorption near edge structure studies of mechanisms of passivity, Electrochim. Acta 47 (19) (2002) 3117–3125, https://doi.org/10.1016/S0013-4686(02)00230-X.
[33] W.J. Chun, K. Asakura, Y. Iwasawa, Polarization-dependent total-reflection fluorescence XAFS study of Mo oxides on a rutile TiO_2 (110) single crystal surface, J. Phys. Chem. B 102 (45) (1998) 9006–9014, https://doi.org/10.1021/jp9820368.
[34] A.N. Mansour, C.A. Melendres, J. Wong, *In situ* X-ray absorption spectroscopic study of electrodeposited nickel oxide films during redox reactions, J. Electrochem. Soc. 145 (4) (1998) 1121–1125, https://doi.org/10.1149/1.1838426.
[35] J. Kruger, G.G. Long, M. Kuriyama, A.I. Goldman, Structural studies of passive films using surface exafs. Passivity of Metals and Semiconductors, Elsevier, 1983, pp. 163–168, https://doi.org/10.1016/B978-0-444-42252-1.50031-X.

[36] G. Falkenberg, G. Pepponi, C. Streli, P. Wobrauschek, Comparison of conventional and total reflection excitation geometry for fluorescence X-ray absorption spectroscopy on droplet samples, Spectrochim. Acta B At. Spectrosc. 58 (12) (2003) 2239–2244, https://doi.org/10.1016/j.sab.2003.06.006.
[37] U. Welzel, J. Ligot, P. Lamparter, A.C. Vermeulen, E.J. Mittemeijer, Stress analysis of polycrystalline thin films and surface regions by X-ray diffraction, J. Appl. Crystallogr. 38 (1) (2005) 1–29, https://doi.org/10.1107/S0021889804029516.
[38] A.V. Vinogradov, N.N. Zorev, I.V. Kozhevnikov, I.G. Yakushkin, Phenomenon of total external reflection of x rays, Zh. Eksp. Teor. Fiz., 89 (1985) 2124-2132, retrieved from http://jetp.ras.ru/cgi-bin/dn/e_062_06_1225.pdf.
[39] H. Abe, Y. Niwa, M. Kimura, A Surface sensitive hard X-ray spectroscopic Method applied to observe the surface layer reduction reaction of Co oxide to Co metal, Phys. Chem. Chem. Phys. 22 (43) (2020) 24974–24977, https://doi.org/10.1039/D0CP02155E.
[40] H. Abe, Y. Niwa, Y. Takeichi, M. Kimura, *In situ* TREXS observation of surface reduction reaction of NiO film with ~2 Nm surface sensitivity, Chem. Rec. 19 (7) (2019) 1457–1461, https://doi.org/10.1002/tcr.201800197.
[41] J.S. Kim, C.H. Chang, K.Y. Kim, *In situ* Xray Absorption spectroscopic study of oxide film on Fe alloy, Phys. Scr. 564 (2005), https://doi.org/10.1238/Physica.Topical.115a00564.
[42] P. Keil, D. Lützenkirchen-Hecht, Surface-sensitive reflection-mode EXAFS from layered sample systems: the influence of surface and interface roughness, J. Synchrotron Radiat. 16 (4) (2009) 443–454, https://doi.org/10.1107/S0909049509015684.
[43] D. Lützenkirchen-Hecht, J. Stötzel, J. Just, O. Müller, B. Bornmann, R. Frahm, Time-Resolved grazing incidence X-ray absorption spectroscopy for the *in situ* investigation of the initial stages of sputter-deposited copper thin films, Phys. Status Solidi A 219 (9) (2022) 2100514, https://doi.org/10.1002/pssa.202100514.
[44] D. Hecht, P. Borthen, H.H. Strehblow, An X-ray absorption fine structure study of the initial stages of the anodic oxidation of silver, Surf. Sci. 365 (2) (1996) 263–277, https://doi.org/10.1016/0039-6028(96)00710-8.
[45] G. Martens, P. Rabe, The extended X-ray absorption fine structure in the reflectivity at the K edge of Cu, J. Phys. C Solid State Phys. 14 (10) (1981) 1523–1534, https://doi.org/10.1088/0022-3719/14/10/020.
[46] G. Martens, P. Rabe, N. Schwentner, A.I Werner, Extended-x-ray-absorption fine-structure (EXAFS) studies applied to the investigation of Cu-O, Cu-N, and Cu-Br bond lengths, Phys. Rev. B 17 (4) (1978) 1481–1488, https://doi.org/10.1103/PhysRevB.17.1481.
[47] D. Hecht, P. Borthen, H.H. Strehblow, *In situ* examination of anodic silver oxide films by EXAFS in the reflection mode, J. Electroanal. Chem. 381 (1–2) (1995) 113–121, https://doi.org/10.1016/0022-0728(94)03611-6.
[48] D. Lützenkirchen-Hecht, R. Frahm, Structure of reactively sputter deposited tin-nitride thin films: a combined X-ray photoelectron spectroscopy, *in situ* X-ray reflectivity and X-ray absorption spectroscopy study, Thin Solid Films 493 (1–2) (2005) 67–76, https://doi.org/10.1016/j.tsf.2005.07.034.
[49] H. Abe, T. Nakayama, Y. Niwa, H. Nitani, H. Kondoh, M. Nomura, Observation of surface reduction of NiO to Ni by surface-sensitive total reflection X-ray spectroscopy using kramers–kronig relations, Jpn. J. Appl. Phys. 55 (6) (2016) 062401, https://doi.org/10.7567/JJAP.55.062401.
[50] S. Pizzini, K.J. Roberts, G.N. Greaves, N. Harris, P. Moore, E. Pantos, R.J. Oldman, Instrumentation for glancing angle X-ray absorption spectroscopy on the synchrotron radiation source, Rev. Sci. Instrum. 60 (7) (1989) 2525–2528, https://doi.org/10.1063/1.1140719.
[51] S.M. Heald, EXAFS at grazing incidence: data collection and analysis, Rev. Sci. Instrum. 63 (1) (1992) 873–878, https://doi.org/10.1063/1.1142632.
[52] L. Bosio, R. Cortes, A. Defrain, M. Froment, EXAFS from measurements of X-ray reflectivity on passivated electrodes, J. Electroanal. Chem. 180 (1–2) (1984) 265–271, https://doi.org/10.1016/0368-1874(84)83585-6.
[53] L. Bosio, R. Cortès, P. Delichère, M. Froment, S. Joiret, EXAFS study of passive films on Ni and Ni-Mo alloy electrodes, Surf. Interface Anal. 12 (7) (1988) 380–384, https://doi.org/10.1002/sia.740120703.
[54] F. Benzi, I. Davoli, M. Rovezzi, F. d'Acapito, A new procedure for the quantitative analysis of extended x-ray absorption fine structure data in total reflection geometry, Rev. Sci. Instrum. 79 (10) (2008) 103902, https://doi.org/10.1063/1.2991111.
[55] B. Ravel, M. Newville, Athena, artemis, hephaestus: data analysis for X-ray absorption spectroscopy using ifeffit, J. Synchrotron Radiat. 12 (2005) 537–541, https://doi.org/10.1107/S0909049505012719.
[56] W. Linpé, G.S. Harlow, A. Larsson, G. Abbondanza, L. Rämisch, S. Pfaff, J. Zetterberg, J. Evertsson, E. Lundgren, An electrochemical cell for 2-dimensional surface optical reflectance during anodization and cyclic voltammetry, Rev. Sci. Instrum. 91 (4) (2020) 044101, https://doi.org/10.1063/1.5133905.
[57] I. Kretzmer, E.M. Stuve, Electrochemical oxide growth on nickel and commercial nickel alloys: influence of chromium and molybdenum, J. Electrochem. Soc. 170 (6) (2023) 066502, https://doi.org/10.1149/1945-7111/acd7a6.
[58] L. Magnier, G. Cossard, V. Martin, C. Pascal, V. Roche, E. Sibert, I. Shchedrina, R. Bousquet, V. Parry, M. Chatenet, Fe–Ni-based alloys as highly active and low-cost oxygen evolution reaction catalyst in alkaline media, Nat. Mater. (2024), https://doi.org/10.1038/s41563-023-01744-5.
[59] S. Yang, D.G.H. Hetterscheid, Redefinition of the active species and the mechanism of the oxygen evolution reaction on gold oxide, ACS Catal. 10 (21) (2020) 12582–12589, https://doi.org/10.1021/acscatal.0c03548.
[60] U. Zhumaev, A.V. Rudnev, J.F. Li, A. Kuzume, T.H. Vu, T. Wandlowski, Electro-oxidation of Au(111) in contact with aqueous electrolytes: new insight from *in situ* vibration spectroscopy, Electrochim. Acta 112 (2013) 853–863, https://doi.org/10.1016/j.electacta.2013.02.105.
[61] G. Zwaschka, I. Nahalka, A. Marchioro, Y. Tong, S. Roke, R.K. Campen, Imaging the heterogeneity of the oxygen evolution reaction on gold electrodes operando: activity is highly local, ACS Catal. 10 (11) (2020) 6084–6093, https://doi.org/10.1021/acscatal.0c01177.
[62] M.L. Foresti, A. Pozzi, M. Innocenti, G. Pezzatini, F. Loglio, E. Salvietti, A. Giusti, F. D'Anca, R. Felici, F. Borgatti, *In situ* X-ray analysis under controlled potential conditions: an innovative setup and its application to the investigation of ultrathin films electrodeposited on Ag(111), Electrochim. Acta 51 (25) (2006) 5532–5539, https://doi.org/10.1016/j.electacta.2006.02.031.
[63] W.A. Caliebe, V. Murzin, A. Kalinko, M. Görlitz, High-flux XAFS-beamline P64 at PETRA III, AIP Conf. Proc. 2054 (2019) 060031, https://doi.org/10.1063/1.5084662.
[64] B.L. Henke, E.M. Gullikson, X-ray interactions: photoabsorption, scattering, transmission, and reflection at E=50-30000 eV, Z=1-92, At. Data Nucl. Data Tables 54 (2) (1983) 181–342, https://doi.org/10.1006/adnd.1993.1013.
[65] A. Larsson, G. D'Acunto, M. Vorobyova, G. Abbondanza, U. Lienert, Z. Hegedüs, A. Preobrajenski, L.R. Merte, J. Eidhagen, A. Delblanc, J. Pan, E. Lundgren, Thickness and composition of native oxides and near-surface regions of Ni superalloys, J. Alloys Compd. 895 (2022) 162657, https://doi.org/10.1016/j.jallcom.2021.162657.
[66] J. Eidhagen, A. Larsson, A. Preobrajenski, A. Delblanc, E. Lundgren, J. Pan, Synchrotron XPS and electrochemical study of aging effect on passive film of Ni alloys, J. Electrochem. Soc. 170 (2) (2023) 021506, https://doi.org/10.1149/1945-7111/acba4b.
[67] J.L. Alfke, A. Müller, A.H. Clark, A. Cervellino, M. Plodinec, A. Comas-Vives, C. Copéret, O.V. Safonova, BCC-Cu nanoparticles: from a transient to a stable allotrope by tuning size and reaction conditions, Phys. Chem. Chem. Phys. 24 (39) (2022) 24429–24438, https://doi.org/10.1039/D2CP03593F.
[68] T. Zhao, X. Shen, Y. Wang, R.K. Hocking, Y. Li, C. Rong, K. Dastafkan, Z. Su, C. Zhao, *In situ* reconstruction of V-doped Ni $_2$ P pre-catalysts with tunable electronic structures for water oxidation, Adv. Funct. Mater. 31 (25) (2021) 2100614, https://doi.org/10.1002/adfm.202100614.
[69] S.Y. Lee, H.J. Oh, M. Kim, H.S. Cho, Y.K. Lee, Insights into enhanced activity and durability of hierarchical Fe-doped Ni(OH)2/Ni catalysts for alkaline oxygen evolution reaction: *in situ* XANES studies, Appl. Catal. B Environ 324 (2023) 122269, https://doi.org/10.1016/j.apcatb.2022.122269.
[70] O. Diaz-Morales, D. Ferrus-Suspedra, M.T.M Koper, The importance of nickel oxyhydroxide deprotonation on its activity towards electrochemical water oxidation, Chem. Sci. 7 (4) (2016) 2639–2645, https://doi.org/10.1039/C5SC04486C.
[71] B.S. Yeo, A.T. Bell, *In situ* Raman study of nickel oxide and gold-supported nickel oxide catalysts for the electrochemical evolution of oxygen, J. Phys. Chem. C 116 (15) (2012) 8394–8400, https://doi.org/10.1021/jp3007415.
[72] G. Tremiliosi-Filho, L.H. Dall'Antonia, G. Jerkiewicz, Limit to extent of formation of the quasi-two-dimensional oxide state on Au electrodes, J. Electroanal. Chem. 422 (1–2) (1997) 149–159, https://doi.org/10.1016/S0022-0728(96)04896-6.
[73] J.H.K. Pfisterer, M. Baghernejad, G. Giuzio, K.F. Domke, Reactivity mapping of nanoscale defect chemistry under electrochemical reaction conditions, Nat. Commun. 10 (1) (2019) 5702, https://doi.org/10.1038/s41467-019-13692-3.
[74] R. Zeis, T. Lei, K. Sieradzki, J. Snyder, J. Erlebacher, Catalytic reduction of oxygen and hydrogen peroxide by nanoporous gold, J. Catal. 253 (1) (2008) 132–138, https://doi.org/10.1016/j.jcat.2007.10.017.
[75] S.Y. Chang, A. Uehara, S.G. Booth, K. Ignatyev, J.F.W. Mosselmans, R.A.W. Dryfe, S.L.M Schroeder, Structure and bonding in Au(I) chloride species: a critical examination of X-ray absorption spectroscopy (XAS) data, RSC Adv 5 (9) (2015) 6912–6918, https://doi.org/10.1039/C4RA13087A.
[76] A. Pantelouris, G. Kueper, J. Hormes, C. Feldmann, M. Jansen, Anionic Gold in Cs3AuO and Rb3AuO Established by X-Ray Absorption Spectroscopy, J. Am. Chem. Soc. 117 (47) (1995) 11749–11753, https://doi.org/10.1021/ja00152a016.
[77] J. Bansmann, G. Kučerová, A.M. Abdel-Mageed, A. Abd El-Moemen, R.J. Behm, Influence of *Re*-activation and ongoing CO oxidation reaction on the chemical and electronic properties of Au on a Au/CeO 2 catalyst: a XANES study at the Au L III edge, J. Electron Spectrosc. Relat. Phenom. 220 (2017) 86–90, https://doi.org/10.1016/j.elspec.2017.01.002.
[78] T. Weber, V. Vonk, M.J.S. Abb, J. Evertsson, A. Stierle, E. Lundgren, H. Over, *In situ* synchrotron-based studies of IrO $_2$ (110)–TiO $_2$ (110) under Harsh acidic water splitting conditions: anodic stability and radiation damages, J. Phys. Chem. C 126 (48) (2022) 20243–20250, https://doi.org/10.1021/acs.jpcc.2c06429.